Available online at www.sciencedirect.com
ScienceDirect
Journal of Computational Physics 220 (2006) 383–393
JOURNAL OF COMPUTATIONAL PHYSICS
www.elsevier.com/locate/jcp

A brick-tetrahedron finite-element interface with stable hybrid explicit–implicit time-stepping for Maxwell's equations

D. Degerfeldt *, T. Rylander

Chalmers University of Technology, Computational Technology Group, SE-412 96 Göteborg, Sweden

Received 6 March 2006; accepted 16 May 2006
Available online 7 July 2006

Abstract

A new brick-tetrahedron finite-element interface with stable hybrid explicit–implicit time-stepping for Maxwell's equations is described and tested. The tetrahedrons are connected directly to the bricks, as opposed to previous curl-conforming formulations that use an intermediate layer of pyramids. The electric field is expanded in linear edge elements, which yields a discontinuous tangential electric field at the brick-tetrahedron interface and this discontinuity is treated by Nitsche's method. In addition, tangential continuity for an arbitrary constant electric field is imposed in the strong sense at the interface, which makes it possible to avoid penalization that perturbs the frequency spectrum. This hybridization preserves the null-space of the curl–curl operator and is free from non-physical spurious modes, which is confirmed by numerical tests. The implicit Newmark time-stepping scheme is employed for the tetrahedrons, which allows for local mesh refinement without reduced time-step. For the brick elements, spatial lumping and explicit time-stepping is employed, which yields the standard finite-difference time-domain scheme. Furthermore, we prove that the explicit–implicit time-stepping employed at the hybrid interface is stable for time-steps up to the Courant limit of the explicitly time-stepped bricks. Second order of convergence is achieved for field solutions without singular behavior. The reflection from the brick-tetrahedron interface is small and scattering from a thin layer of tetrahedrons indicates levels at approximately −49 dB for a resolution of 14 cells per wavelength.

Keywords: Finite-difference time-domain; Finite-element methods; Hybrid methods; Discontinuous Galerkin; Nitsche's method; Maxwell's equations; Explicit–implicit time-stepping; Stability analysis

1. Introduction

The finite-difference time-domain (FDTD) scheme [1,2] is widely used for numerical modeling of electromagnetic problems. Its basic formulation uses structured (Cartesian) grids which makes it simple to understand, easy to implement and computationally efficient in terms of floating point operations and memory requirements. However, modeling of oblique and curved material-boundaries suffers from the staircase

* Corresponding author. Tel.: +46 31 772 1885.
E-mail address: david.degerfeldt@chalmers.se (D. Degerfeldt).

0021-9991/$ - see front matter © 2006 Elsevier Inc. All rights reserved.
doi:10.1016/j.jcp.2006.05.016

approximation, which can introduce significant errors [3]. In contrast, the finite-element method (FEM) [4] can exploit body conforming unstructured meshes, which makes it well suited for complex geometries and allows for local mesh refinement. Edge elements [5] perform well for Maxwell's equations and the implicit Newmark scheme [6,7] allows for unconditionally stable time-stepping. However, the FEM is computationally more expensive as compared to the FDTD scheme.

Given these two complementary techniques, it is attractive to use the efficient FDTD scheme in homogeneous regions combined with the flexible FEM in the vicinity of complex boundaries or regions with rapid field variations. There is a number of alternatives on how to connect the electromagnetic field in the FDTD region with the FEM field solution. One approach is to use interpolation at the FEM–FDTD interface [8,9] or in a region where the FDTD and FEM discretizations overlap [10,11]. In general, interpolation yields non-symmetric discrete operators and fails to preserve the reciprocity of Maxwell's equations. The lack of reciprocity at the interface often results in late-time instabilities due to the complex eigenvalues associated with the non-symmetric matrix operators. The unphysical late-time instabilities can be artificially damped by e.g. spectral filtering [12]. The finite-volume method in the time domain has also been used to connect unstructured grids to an FDTD scheme [13] and the inherent late-time instabilities can be treated with a dissipative time-integration scheme [14]. For weakly damped systems however, the artificial damping required for stable time-stepping may dominate the physical damping phenomena of interest. Pyramidal elements [15] can be used to construct a stable curl-conforming hybrid [16,17] that connects the FDTD scheme with the FEM formulated on an unstructured grid of tetrahedrons. This type of hybridization is free from spurious solutions and its explicit–implicit time-stepping algorithm is proven stable [17] for time steps up to the Courant limit for the FDTD scheme without added artificial damping. In practice however, automatic mesh generation that connects bricks, pyramids and tetrahedrons to yield a discretization appropriate for efficient hybrid computations is non-trivial and often very time consuming.

In this paper, we present a new FEM–FDTD hybrid that connects the tetrahedrons in the FEM region directly to the FDTD cells, which eliminates the need for pyramidal elements and its difficulties. Viewed from the FDTD region, the tangential electric field at the FEM–FDTD interface is expressed in terms of rectangular edge elements [18]. On the other hand, the unstructured mesh exploits edge elements on tetrahedrons [4], which on the interface spans a different space for the tangential electric field. Consequently, this type of formulation allows for a discontinuous tangential electric field at the interface. We couple the FDTD and FEM field solutions at the interface by means of Nitsche's method [19], which is an intermediate in-between the Lagrange multiplier method and the penalization method. Nitsche's method can also be related to discontinuous Galerkin methods [20–22], where penalization is employed to weakly enforce continuous tangential electric field at all cell faces in the grid. Here, we constrain the degrees of freedom at the interface such that an arbitrary constant electric field has a continuous tangential component. This hybrid interface preserves the null-space of the curl–curl operator and is free from spurious solutions. We present a proof of stability for the hybrid interface with explicit–implicit time-stepping and numerical results that demonstrate a performance similar to previous curl-conforming hybridizations [16,17].

2. The FEM–FDTD hybrid formulation

The computational domain is discretized by brick shaped hexahedrons in homogeneous regions and tetrahedrons close to curved or oblique boundaries. Tetrahedrons can also be useful for local refinement, e.g. in regions where rapid field variations are expected. The regions discretized with bricks and tetrahedrons are referred to as Ω^{hex} and Ω^{tet}, respectively. Fig. 1 shows how the bricks and tetrahedrons are connected at the interface Γ between Ω^{hex} and Ω^{tet}. Each tetrahedron face that connects to the interface Γ shares two edges with its neighboring brick and, as a consequence, the third edge coincides with the diagonal of the rectangular face of the brick.

2.1. FEM for the brick-tetrahedron interface

We let $\hat{n}$ be the unit normal vector that points out from Ω^{hex} and assume constant material parameters. Maxwell's equations can then be formulated as

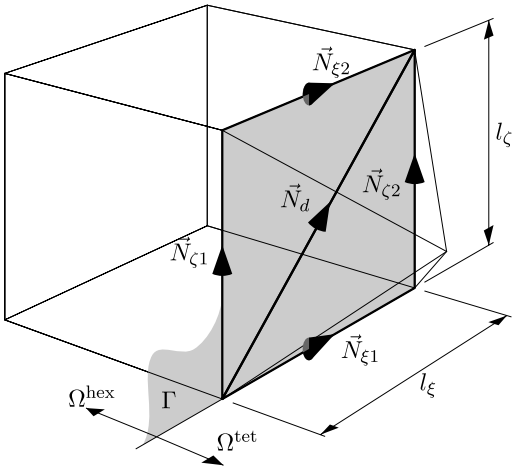

Fig. 1. A brick connected to two tetrahedrons at the interface between the FDTD and FEM regions. The interface is shaded gray.

$$\nabla \times (\nabla \times \vec{E}) - k^2 \vec{E} = \vec{0} \quad \text{in } \Omega^{\text{hex}} \text{ and } \Omega^{\text{tet}}, \tag{1}$$

$$\hat{n} \times [\![\vec{E}]\!] = \vec{0} \quad \text{on } \Gamma, \tag{2}$$

$$\hat{n} \times [\![\nabla \times \vec{E}]\!] = \vec{0} \quad \text{on } \Gamma, \tag{3}$$

where k is the wave number and $[\![\vec{E}]\!] = \vec{E}^{\text{tet}} - \vec{E}^{\text{hex}}$ is the jump of $\vec{E}$ at the interface Γ. The restriction of $\vec{E}$ to Ω^{hex} and Ω^{tet} is denoted $\vec{E}^{\text{hex}}$ and $\vec{E}^{\text{tet}}$, respectively. In the following, the electric field is expanded in terms of linear edge elements $\vec{N}_i^{\text{hex}}$ on the brick shaped hexahedrons [4] in Ω^{hex} as

$$\vec{E}_h^{\text{hex}} = \sum_i e_i^{\text{hex}} \vec{N}_i^{\text{hex}}, \tag{4}$$

where the sub-index h indicates the cell size. Analogously, linear edge elements $\vec{N}_i^{\text{tet}}$ on tetrahedrons [4] are used as basis functions for the electric field in Ω^{tet}. At the outer boundaries of Ω^{hex} and Ω^{tet} that excludes their common interface Γ, we have $\hat{n} \times \vec{E} = \vec{0}$ but other physically appropriate boundary conditions are feasible given the application at hand.

In a conventional curl-conforming representation based on edge elements, continuous tangential electric field at element boundaries is enforced by the discrete space [5]. Here however, the tangential field component can be discontinuous at the brick-tetrahedron interface and therefore we use Nitsche's method [19] to arrive at the weak formulation

$$\begin{aligned}
&\left(\nabla \times \vec{w}_h^{\text{tet}}, \nabla \times \vec{E}_h^{\text{tet}}\right)_{\Omega^{\text{tet}}} + \left(\nabla \times \vec{w}_h^{\text{hex}}, \nabla \times \vec{E}_h^{\text{hex}}\right)_{\Omega^{\text{hex}}} + \left(\hat{n} \times [\![\vec{w}_h]\!], \nabla \times \{\!\{\vec{E}_h\}\!\}_\alpha\right)_\Gamma \\
&+ \left(\nabla \times \{\!\{\vec{w}_h\}\!\}_\alpha, \hat{n} \times [\![\vec{E}_h]\!]\right)_\Gamma + \gamma \left(\hat{n} \times [\![\vec{w}_h]\!], \frac{1}{h} \hat{n} \times [\![\vec{E}_h]\!]\right)_\Gamma - k^2 \left(\vec{w}_h^{\text{tet}}, \vec{E}_h^{\text{tet}}\right)_{\Omega^{\text{tet}}} - k^2 \left(\vec{w}_h^{\text{hex}}, \vec{E}_h^{\text{hex}}\right)_{\Omega^{\text{hex}}} = 0,
\end{aligned} \tag{5}$$

where the test function is denoted $\vec{w}_h$, h is the element size and γ is a positive constant that can be used to avoid an indefinite stiffness matrix [19]. We use the average $\{\!\{\vec{w}_h\}\!\}_\alpha = \alpha \vec{w}_h^{\text{hex}} + (1-\alpha)\vec{w}_h^{\text{tet}}$ and the inner products $(\vec{a}, \vec{c})_\Omega = \int_\Omega \vec{a} \cdot \vec{c}\, \mathrm{d}v$ and $(\vec{a}, \vec{c})_\Gamma = \int_\Gamma \vec{a} \cdot \vec{c}\, \mathrm{d}s$.

The weak formulation (5) is consistent with the original problem in the sense that it is satisfied by the solution of Maxwell's equations (1)–(3). Integration by parts of the curl–curl operator gives the interface term $(\hat{n} \times [\![\vec{w}_h]\!], \nabla \times \{\!\{\vec{E}_h\}\!\}_\alpha)_\Gamma$, which is a natural consequence given the discontinuous tangential electric field at the interface. The two additional interface terms are introduced since $(\nabla \times \{\!\{\vec{w}_h\}\!\}_\alpha, \hat{n} \times [\![\vec{E}_h]\!])_\Gamma$ yields symmetry and $\gamma(\hat{n} \times [\![\vec{w}_h]\!], \frac{1}{h}\hat{n} \times [\![\vec{E}_h]\!])_\Gamma$ allows for stabilization of the stiffness matrix.

Galerkin's method is applied to the weak formulation (5) and its matrix representation is

$$(\mathbf{S} + \mathbf{S}^A + \gamma \mathbf{S}^B)\mathbf{e} = k^2 \mathbf{M}\mathbf{e}, \tag{6}$$

where **e** is the vector of unknowns and

$$\mathbf{S}_{ij} = \left(\nabla \times \vec{N}_i^{\text{tet}}, \nabla \times \vec{N}_j^{\text{tet}}\right)_{\Omega^{\text{tet}}} + \left(\nabla \times \vec{N}_i^{\text{hex}}, \nabla \times \vec{N}_j^{\text{hex}}\right)_{\Omega^{\text{hex}}}, \tag{7}$$

$$\mathbf{S}_{ij}^{A} = \left(\hat{n} \times [\![\vec{N}_i]\!], \nabla \times \vec{N}_j^{\text{hex}}\right)_{\Gamma} + \left(\nabla \times \vec{N}_i^{\text{hex}}, \hat{n} \times [\![\vec{N}_j]\!]\right)_{\Gamma}, \tag{8}$$

$$\mathbf{S}_{ij}^{B} = \left(\hat{n} \times [\![\vec{N}_i]\!], \frac{1}{h}\hat{n} \times [\![\vec{N}_j]\!]\right)_{\Gamma}, \tag{9}$$

$$\mathbf{M}_{ij} = \left(\vec{N}_i^{\text{tet}}, \vec{N}_j^{\text{tet}}\right)_{\Omega^{\text{tet}}} + \left(\vec{N}_i^{\text{hex}}, \vec{N}_j^{\text{hex}}\right)_{\Omega^{\text{hex}}}, \tag{10}$$

where we have chosen $\alpha = 1$. (It is common to choose $\alpha = 1/2$ in discontinuous Galerkin formulations [21,22].)

For a curl-conforming formulation, the stiffness matrix is positive semi-definite and its null-space is spanned by the electrostatic field solutions $\vec{E} = -\nabla\phi$. Here, the stiffness matrix is $\mathbf{S} + \mathbf{S}^A + \gamma\mathbf{S}^B$, where $\mathbf{S}$ is positive semi-definite and $\mathbf{S}^B$ is positive definite. The curl–curl operator can be stabilized by a sufficiently large γ, which is a necessary countermeasure if the combination $\mathbf{S} + \mathbf{S}^A$ is indefinite. However, $\gamma > 0$ may also imply that the discretized curl–curl operator yields a non-zero result (and eigenfrequency) when applied to a static electric field $\vec{E} = -\nabla\phi$. The work by Hansbo and Larson [23] on the discontinuous Galerkin method and the Crouzeix–Raviart element demonstrates that the terms that correspond to Eq. (8) in elasticity vanish for the linear approximation since its jump averages to zero on inter-elemental boundaries. The present situation with edge elements is somewhat more involved, e.g. the spatial derivative of the linear edge elements $\vec{N}_i^{\text{hex}}$ that features in Eq. (8) is piecewise linear on Γ. As opposed to the conventional application of Nitsche's method, we proceed from this point in the following manner.

We set $e_i^{\text{hex}} = e_i^{\text{tet}} = e_i$ for the edges $i = \zeta 1, \zeta 2, \xi 1$ and $\xi 2$ in Fig. 1. For the degree of freedom e_d^{tet} associated with the edge that lie on the diagonal of the brick's face, we enforce

$$e_d^{\text{tet}} = \frac{l_\xi}{l_d}\frac{e_{\xi 1} + e_{\xi 2}}{2} + \frac{l_\zeta}{l_d}\frac{e_{\zeta 1} + e_{\zeta 2}}{2}, \tag{11}$$

where l_i is the length of edge i. This yields a continuous tangential component at the interface Γ for an arbitrary constant electric field and a piecewise linear representation of the scalar potential ϕ that spans the null-space $\vec{E} = -\nabla\phi$ of the operator $\mathbf{S} + \mathbf{S}^A$. Wu and Itoh [8] and Monorchio et al. [24] used Eq. (11) to interpolate the solution in the FDTD region and construct a Dirichlet boundary condition for the FEM region, in a manner that gives a non-symmetric operator at the interface and time-stepping instabilities. Here, we use Eq. (11) differently in the sense that we eliminate the degree of freedom e_d^{tet} associated with the diagonal. Our approach gives a constraint that is implemented by means of the modified basis functions

$$\widetilde{\vec{N}_{\zeta 1}^{\text{tet}}} = \vec{N}_{\zeta 1}^{\text{tet}} + \frac{l_\zeta}{2l_d}\vec{N}_d^{\text{tet}}, \tag{12}$$

$$\widetilde{\vec{N}_{\zeta 2}^{\text{tet}}} = \vec{N}_{\zeta 2}^{\text{tet}} + \frac{l_\zeta}{2l_d}\vec{N}_d^{\text{tet}}, \tag{13}$$

$$\widetilde{\vec{N}_{\xi 1}^{\text{tet}}} = \vec{N}_{\xi 1}^{\text{tet}} + \frac{l_\xi}{2l_d}\vec{N}_d^{\text{tet}}, \tag{14}$$

$$\widetilde{\vec{N}_{\xi 2}^{\text{tet}}} = \vec{N}_{\xi 2}^{\text{tet}} + \frac{l_\xi}{2l_d}\vec{N}_d^{\text{tet}} \tag{15}$$

associated with the interface.

After some rather lengthy calculations based on the modified basis functions (12)–(15), the surface integrals (8) give $\mathbf{S}^A = \mathbf{0}$ and the resulting stiffness matrix is $\mathbf{S} + \gamma\mathbf{S}^B$. Finally, we set $\gamma = 0$ to avoid electrostatic solutions with non-zero eigenfrequencies and the discretized problem that corresponds to Eqs. (1)–(3) is

$$\mathbf{Se} = k^2\mathbf{Me}. \tag{16}$$

This discretization preserves the reciprocity of Maxwell's equations, which is an essential prerequisite for stable time-stepping [17].

2.2. Temporal discretization

The time-domain problem derived from Eq. (16) is time-stepped by the algorithm [17]

$$\sum_{k=1}^{K}\left(\mathbf{S}_k\left[\theta_k\mathbf{e}^{(n+1)}+(1-2\theta_k)\mathbf{e}^{(n)}+\theta_k\mathbf{e}^{(n-1)}\right]+\frac{1}{(c\Delta t)^2}\mathbf{M}_k\left[\mathbf{e}^{(n+1)}-2\mathbf{e}^{(n)}+\mathbf{e}^{(n-1)}\right]\right)=0, \tag{17}$$

where c is the speed of light, K is the number of elements and $\mathbf{S}_k$ is the contribution from element k to the stiffness matrix such that $\mathbf{S}=\sum_{k=1}^{K}\mathbf{S}_k$. The same partitioning is applied to the mass matrix $\mathbf{M}$. The time-stepping scheme (17) associates the implicitness parameter θ_k with the elements. For the tetrahedrons, we use $\theta_k=1/4$ and this choice gives the unconditionally stable Newmark scheme [6,7]. For the bricks, we set $\theta_k=0$ and employ spatial lumping, which yields the explicit FDTD time-stepping scheme [18]. Thus, the two time-stepping schemes are hybridized at the interface. This type of FEM that combines exact integration with lumping based on trapezoidal integration is also known as tunable integration [25].

2.3. Proof of stability

Here, we present the outline for a proof of stability for the hybrid formulation. Further details can be found in Ref. [17], where it is applied to a curl-conforming hybrid. On a brick element, the eigenvalue problem (16) yields the quadratic form

$$\mathbf{e}^H\mathbf{S}_k\mathbf{e}\leqslant\lambda_{\max}\mathbf{e}^H\mathbf{M}_k\mathbf{e}, \tag{18}$$

where $\mathbf{e}$ is the vector of unknowns, $\mathbf{e}^H$ is its complex transpose and

$$\lambda_{\max}=4\left(\frac{1}{h_x^2}+\frac{1}{h_y^2}+\frac{1}{h_z^2}\right), \tag{19}$$

with the cell dimensions denoted h_x, h_y and h_z. This gives the Courant condition $c\Delta t\leqslant 2/\sqrt{\lambda_{\max}}$ for the FDTD time-step [2,26].

We prove stability of the hybrid by the von Neumann method [26]. Let $\tilde{\mathbf{e}}$ be a complex eigenmode of (17) and assume it has a growth factor ρ such that $\mathbf{e}^{(n)}=\rho^n\tilde{\mathbf{e}}$. Stability is equivalent to $|\rho|\leqslant 1$ for all modes and the substitution $\rho=(1+\zeta)/(1-\zeta)$ gives the stability condition $\Re\{\zeta\}\leqslant 0$. The time-stepping scheme (17) yields the quadratic form

$$\sum_{k=1}^{K}\tilde{\mathbf{e}}^H\mathbf{S}_k\tilde{\mathbf{e}}=-\zeta^2\sum_{k=1}^{K}\tilde{\mathbf{e}}^H\left[\frac{4}{(c\Delta t)^2}\mathbf{M}_k+\mathbf{S}_k(4\theta_k-1)\right]\tilde{\mathbf{e}} \tag{20}$$

for mode $\tilde{\mathbf{e}}$, where ζ^2 must be real since all matrices are Hermitian. The contribution from the implicit elements to the sum on the right-hand side of Eq. (20) is positive if $\theta_k\geqslant 1/4$ for these elements. Eq. (18) implies that the contribution from the explicit elements is non-negative if the Courant condition is satisfied. Thus, the hybrid is stable for time steps up to the Courant limit if $\theta_k\geqslant 1/4$ for the tetrahedrons.

3. Numerical results

3.1. Resonance frequencies for cubic cavity

As a first test case, we compute the resonance frequencies for a cubic cavity of side a. The cavity is divided into a basic grid of cube shaped cells of side $h=a/N$, where N is a positive, even integer. The computational mesh consists of the cubes in the upper half of the cavity and a mesh of tetrahedrons is constructed in the lower half by splitting each cube in that region into 12 tetrahedrons. The hybrid mesh for $N=4$ is shown in Fig. 2.

The generalized eigenvalue problem (16) is solved for $N=6$ and Fig. 3 shows the 10 lowest non-zero resonance frequencies by circles together with the expected analytical values shown by crosses. The multiplicity of the lowest eigenmodes is correct and there is no spectral pollution. Furthermore, the number of zero eigenvalues, that all stem from electrostatic modes, equals the number of interior nodes in the mesh as expected.

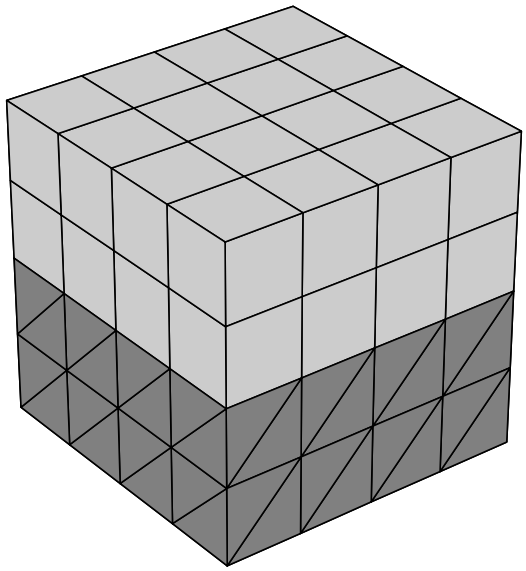

Fig. 2. Cubic cavity discretized with cubes in the upper half and tetrahedrons in the lower half.

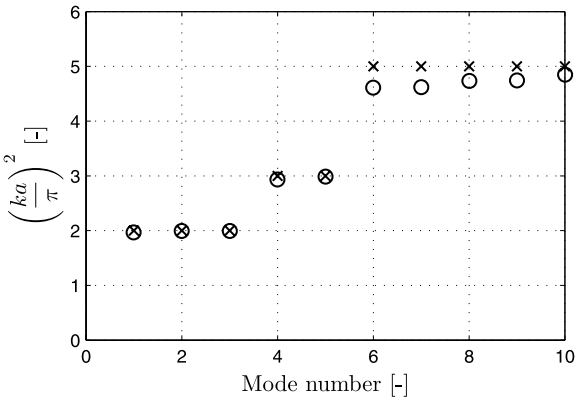

Fig. 3. The 10 lowest non-zero normalized resonance frequencies of a cubic cavity with perfectly conducting metal walls. Eigenvalues computed with the new hybrid are shown by circles and the analytical values are shown by crosses.

Fig. 4 shows the relative error for the eigenfrequencies as a function of spatial resolution for $N/2 = 1, 2, \ldots, 8$. Second order convergence is achieved, which is expected for a FEM with linear elements applied to a problem with a regular solution. These results are similar to the results in Ref. [16], where the same problem is solved by a curl-conforming hybrid formulation with pyramidal elements.

3.2. Reflections from tetrahedron layer

One possible drawback of hybrid formulations is the reflection that occurs at the interface between the brick and tetrahedron meshes. Here, we study such reflections for a thin cross-sectional layer of tetrahedrons placed in a homogeneous rectangular waveguide discretized by the FDTD scheme. A TE_{10}-mode is inserted at one end of the waveguide and propagated through the waveguide. Here, the reflection coefficient is chosen as the ratio of the maximum amplitude of the reflected and transmitted waves. The waveguide with the implicit region indicated and the incident wave is shown in Fig. 5.

In the following computations, the excitation amplitude for the TE_{10}-mode is $\exp\left[-(t-t_0)^2/d_0^2\right]\sin(2\pi f t)$, where $t_0 = 6.25/f_c$, $d_0 = 2.5/f_c$, $f = \sqrt{2}f_c$ and f_c is the cutoff frequency for the TE_{10}-mode. The cross-section of

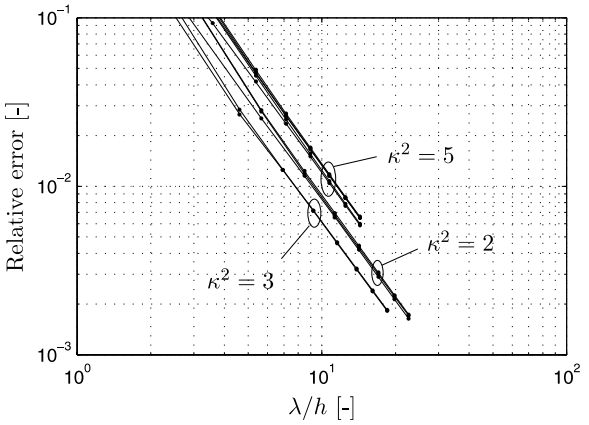

Fig. 4. The relative error for normalized resonance frequencies $\kappa = ka/\pi$ of the 10 lowest modes in a cubic cavity of side a. Second order convergence order is achieved with respect to λ/h, where $\lambda = 2\pi c/\omega$ and the analytical eigenfrequency is ω.

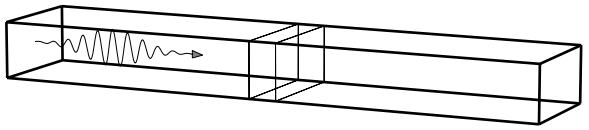

Fig. 5. Schematic view of the waveguide and the incident TE_{10}-mode. The layer in the middle of the waveguide is discretized by tetrahedrons and the rest of the waveguide is discretized by cubes.

the waveguide is discretized by 5×10 FDTD cubes and the implicit region with tetrahedrons is two FDTD cells thick. The power reflection coefficient is shown in Fig. 6 for $1/4 \leqslant \theta \leqslant 1/2$ applied to the tetrahedrons and time steps that satisfy $1/2 \leqslant \sqrt{3}c\Delta t/h \leqslant 1$. The power reflection is almost constant in the region below the -49 dB level contour, where the dominant source of error is related to the spatial discretization. Additional computations for the case when Δt tends to zero with $\theta = 1/4$ shows that the power reflection approaches -49.4 dB, which is 2.5 dB lower than for the curl-conforming hybrid [17]. This reduction is rather constant for time steps up to the Courant limit for $\theta = 1/4$.

Also, we perform a convergence study of the reflection coefficient with respect to the cell size. The dimensions of the waveguide are fixed and the thickness of the implicit tetrahedron layer is $2h$. The time-step is $\Delta t = h/(c\sqrt{3})$ for all resolutions and we use $\theta = 1/4$ for the tetrahedrons. The reflection coefficient is shown in Fig. 7 together with the corresponding results for the curl-conforming hybrid [17], where pyramids are used

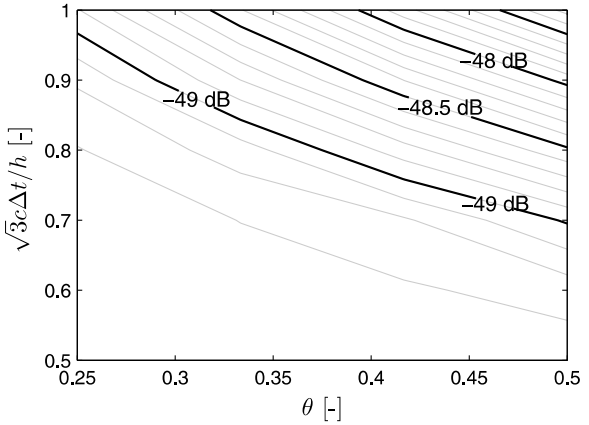

Fig. 6. Contour plot for the power reflection coefficient for 14 cells per wavelength. The thin lines are separated by 0.1 dB.

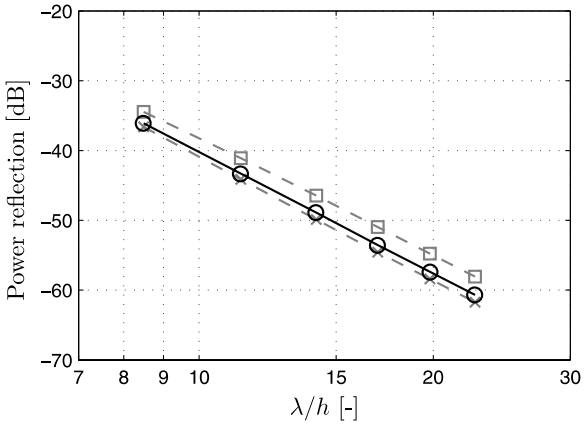

Fig. 7. Power reflection coefficient for $\theta = 1/4$ and $\Delta t = h/(c\sqrt{3})$: new hybrid – solid line with circles; curl-conforming hybrid with exact integration – dashed line with squares; and curl-conforming hybrid with trapezoidal integration – dashed line with crosses.

to connect the FEM tetrahedrons to the FDTD cubes. The new hybrid reduces the reflection coefficient by 2.5 dB as compared to the curl-conforming hybrid with exact integration for the pyramids. In this particular test case, trapezoidal integration employed over the base of the pyramids reduces the reflection for the curl-conforming hybrid. However, it has been demonstrated [17] that trapezoidal integration slightly deteriorates the accuracy when the curl-conforming hybrid is applied to scattering from a perfectly conducting metal sphere. The power reflection coefficient varies as $h^{5.7}$ for both the new and the curl-conforming hybrid [17].

3.3. Resonance frequencies in a cavity containing a sphere

Consider a brick shaped cavity discretized by a hybrid grid that conforms to a small spherical surface. The interior of the sphere and its immediate vicinity is discretized by tetrahedrons while the rest of the cavity is discretized by FDTD cubes of size h. The cavity measures $9h$, $12h$ and $13h$ in the x-, y- and z-directions respectively. The sphere has a radius h and is centered at $(4.5h, 5.5h, 7.5h)$. The grid for the sphere is shown in Fig. 8 together with the interface between the tetrahedrons and the cubes for $y > 4h$.

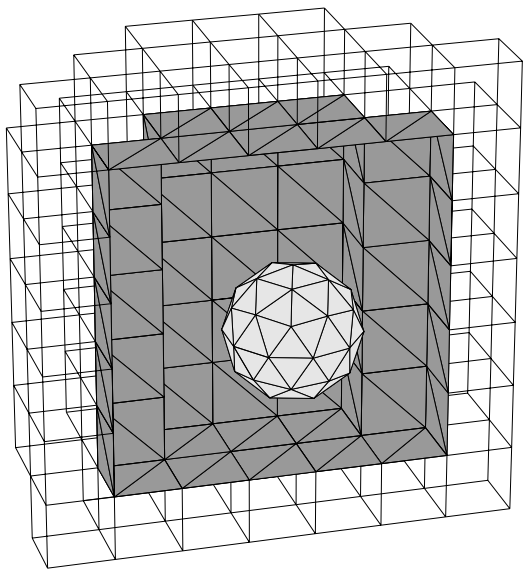

Fig. 8. A section of the implicit grid where the region closest to the sphere is discretized by tetrahedrons. The first layer of cubes outside the tetrahedron region is also shown.

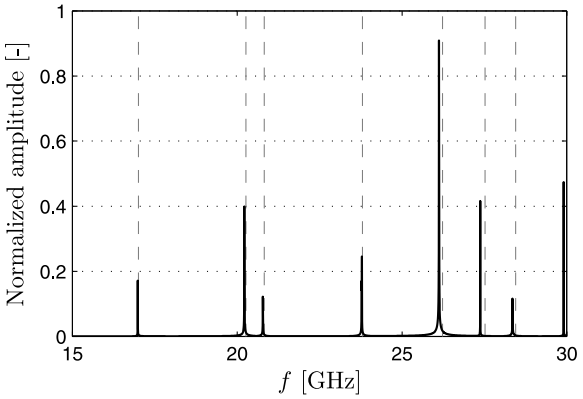

Fig. 9. Spectrum for the empty cavity. Analytical resonance frequencies are shown with vertical dashed lines.

For a homogeneous brick cavity, the analytical eigenfrequencies are available and we study this case with the hybrid grid shown in Fig. 8, where the interior of the sphere is discretized by tetrahedrons. We choose $h = 1$ mm, $\theta = 1/4$ and $\Delta t = h/\left(c\sqrt{3}\right)$ for an empty cavity. A random field distribution is used as the initial condition for the time-stepping. The resonance frequencies are estimated from the peaks found in the Fourier transform of the time-domain solution $\mathbf{e}^{(n)}$. Fig. 9 shows the spectrum computed from a time-domain response of 100,000 time steps, where the lowest oscillations are captured by a set of components in $\mathbf{e}^{(n)}$ that are linearly

Table 1
Resonance frequencies for the empty cavity computed by the new hybrid

Mode indices	f [GHz]		Error [%]
	Hybrid	Exact	
011	16.98	17.00	−0.1
101	20.22	20.26	−0.2
110	20.78	20.82	−0.2
111	23.78	23.80	−0.1
012	26.12	26.23	−0.4
021	27.37	27.52	−0.5
102	28.35	28.45	−0.3
120	29.90	30.03	−0.4
112	31.02	31.07	−0.2
121	32.08	32.16	−0.2

The analytical values and relative errors are also included for comparison.

Table 2
Resonance frequencies for the cavity containing a perfectly conducting metal sphere computed by the new hybrid, a curl-conforming hybrid and a TLM based code

Mode number	f [GHz]		
	New hybrid	Curl-conf. hybrid	TLM
1	16.58	16.56 (−0.11%)	16.64 (0.36%)
2	19.70	19.66 (−0.18%)	19.80 (0.51%)
3	20.23	20.19 (−0.20%)	20.34 (0.54%)
4	23.71	23.69 (−0.07%)	23.73 (0.08%)
5	23.74	23.73 (−0.06%)	23.75 (0.04%)
6	26.06	26.05 (−0.06%)	26.14 (0.31%)
7	27.47	27.46 (−0.02%)	27.56 (0.33%)
8	28.24	28.22 (−0.08%)	28.32 (0.28%)
9	29.91	29.88 (−0.10%)	29.97 (0.20%)

The deviation shown within parentheses is relative to the new hybrid.

combined. The resonance frequencies are determined with high accuracy by means of a Padé approximation fit [26,27] and the first 10 modes are shown in Table 1 together with the expected analytical values. There is no pollution of the spectrum and the deviation from the analytical values is small. As well as the other test cases, this long-run simulation confirms that the new hybrid does not suffer from late-time instabilities.

Next, the sphere is modeled as a perfectly conducting metal object. In this case, no analytical solution exist and we rely on comparisons with other numerical results [16] for verification. Table 2 shows the first few resonances computed by the new hybrid formulation together with the corresponding results obtained by a curl-conforming hybrid [16] and a generalized transmission line method (TLM) [28,29]. The FDTD meshes used for the hybrid computations have $9 \times 12 \times 13$ cells while the basic grid of the TLM computation has $18 \times 24 \times 32$ cells. The results obtained with the new hybrid is in-between the results for the curl-conforming hybrid and the TLM computations for all modes in Table 2.

4. Conclusions

We have presented a new brick-tetrahedron finite-element interface with stable hybrid explicit–implicit time-stepping for Maxwell's equations. The finite-element method (FEM) is employed on a discretization where the tetrahedrons are connected directly to the brick shaped elements. The discontinuity in the tangential electric field at the interface is treated by means of Nitsche's method. For an arbitrary constant electric field, tangential continuity at the interface is enforced in the strong sense. Galerkin's method applied to the self-adjoint Maxwell's equations gives symmetric discretized spatial operators. This construction yields a hybridization that is free from unphysical spurious modes and preserves the null-space of the curl–curl operator. The Newmark scheme applied to the tetrahedrons is combined with an explicit central-difference time-stepping algorithm for the spatially lumped bricks, which is equivalent to the finite-difference time-domain (FDTD) scheme. This construction allows for local mesh refinement in the tetrahedral region and the hybridized FEM–FDTD interface is proven stable up to the Courant limit for the FDTD region.

For a cubic cavity discretized by a hybrid grid, the eigenvalue problem yields accurate resonance frequencies: 1% accuracy for about 10 cells per wavelength; no spectral pollution; correct multiplicity; preserved null-space of the curl–curl operator; and second order of convergence. Scattering from a thin cross-sectional layer of tetrahedrons embedded in a rectangular waveguide discretized by FDTD cubes indicates low reflection from the FEM–FDTD interface: a resolution of 14 cells per wavelength yields approximately -49 dB for the power reflection coefficient and it converges as $h^{5.7}$. The resonance frequencies for a cavity with a hybrid mesh that conforms to a small sphere agree well with the results computed by a curl-conforming hybrid and a generalized transmission line method. A long-run computation with 100,000 time steps show no indication of late-time instabilities. In fact, all tests confirm that the hybrid is robust, accurate and stable.

The brick-tetrahedron interface does not require special elements such as pyramids to connect the tetrahedrons to the FDTD cells. (The edge element basis functions on pyramids are not polynomial, which is unconventional and require special numerical treatment.) From a practical point of view, our new brick-tetrahedron interface simplifies mesh generation considerably without sacrificing stability or accuracy. Tetrahedral grids tailored for efficient hybrid computations can be constructed by commercially available tools, which paves way for automatized computations with parametric geometry representation. This is an important step towards industrial parametric studies, and ultimately optimization, of microwave devices with respect to the geometry.

References

[1] K.S. Yee, Numerical solution of initial boundary value problems involving Maxwell's equations in isotropic media, IEEE Trans. Antennas Propag. 14 (3) (1966) 302–307.
[2] A. Taflove, S.C. Hagness, Computational Electrodynamics: The Finite-Difference Time-Domain Method, third ed., Artech House, Norwood, MA, 2005.
[3] A.C. Cangellaris, D.B. Wright, Analysis of the numerical error caused by the stair-stepped approximation of a conducting boundary in FDTD simulations of electromagnetic phenomena, IEEE Trans. Antennas Propag. 39 (10) (1991) 1518–1525.
[4] J. Jin, The Finite Element Method in Electromagnetics, second ed., John Wiley & Sons, New York, NY, 2002.
[5] J.C. Nédélec, Mixed finite elements in R^3, Numer. Math. 35 (3) (1980) 315–341.

[6] N.M. Newmark, Method of computation for structural dynamics, ASCE – Proc (J. Eng. Mech. Div.) 85 (n EM3, Part 1) (1959) 67–94.
[7] J.-F. Lee, R. Lee, A. Cangellaris, Time-domain finite-element methods, IEEE Trans. Antennas Propag. 45 (3) (1997) 430–442, doi:10.1109/8.558658.
[8] R.-B. Wu, T. Itoh, Hybrid finite-difference time-domain modeling of curved surfaces using tetrahedral edge elements, IEEE Trans. Antennas Propag. 45 (8) (1997) 1302–1309, doi:10.1109/8.611251.
[9] A. Monorchio, R. Mittra, A hybrid finite-element finite-difference time-domain technique for solving complex electromagnetic problems, IEEE Microw. Guid. Wave Lett. 8 (2) (1998) 93–95, doi:10.1109/75.658652.
[10] D. Koh, H.-b. Lee, T. Itoh, A hybrid full-wave analysis of via-hole grounds using finite-difference and finite-element time-domain methods, IEEE Trans. Microw. Theory Tech. 45 (12) (1997) 2217–2223, doi:10.1109/22.643819.
[11] M. El Hachemi, O. Hassan, K. Morgan, D. Rowse, N. Weatherill, A low-order unstructured-mesh approach for computational electromagnetics in the time domain, Philos. Trans. R. Soc. Lond. A, Math. Phys. Eng. Sci. 362 (1816) (2004) 445–469, doi:10.1098/rsta.2003.1330.
[12] C.-T. Hwang, R.-B. Wu, Treating late-time instability of hybrid finite-element/finite-difference time-domain method, IEEE Trans. Antennas Propag. 47 (2) (1999) 227–232, doi:10.1109/8.761061.
[13] D.J. Riley, C.D. Turner, Interfacing unstructured tetrahedron grids to structured-grid FDTD, IEEE Microw. Guid. Wave Lett. 5 (9) (1995) 284–286, doi:10.1109/75.410398.
[14] D.J. Riley, C.D. Turner, VOLMAX: a solid-model-based transient volumetrix Maxwell solver using hybrid grids, IEEE Antennas Propag. Mag. 39 (1) (1997) 20–33, doi:10.1109/74.583516.
[15] F.-X. Zgainski, J.-L. Coulomb, M. Yves, A new family of finite elements: the pyramidal elements, IEEE Trans. Magn. 32 (3) (1996) 1393–1396, doi:10.1109/20.497507.
[16] T. Rylander, A. Bondeson, Stable FEM-FDTD hybrid method for Maxwell's equations, Comput. Phys. Commun. 125 (1) (2000) 75–82, doi:10.1016/S0010-4655(99)00463-4.
[17] T. Rylander, A. Bondeson, Stability of explicit–implicit hybrid time-stepping schemes for Maxwell's equations, J. Comput. Phys. 179 (2) (2002) 426–438, doi:10.1006/jcph.2002.7063.
[18] M.-F. Wong, O. Picon, V.F. Hanna, A finite element method based on Whitney forms to solve Maxwell equations in the time domain, IEEE Trans. Magn. 31 (3) (1995) 1618–1621, doi:10.1109/20.376343.
[19] P. Hansbo, Nitsche's method for interface problems in computational mechanics, GAMM-Mitt 28 (2) (2005) 184–207.
[20] P. Houston, I. Perugia, A. Schneebeli, D. Schötzau, Mixed discontinuous Galerkin approximation of the Maxwell operator: the indefinite case, Math. Model. Numer. Anal. 39 (4) (1995) 727–753.
[21] P. Houston, I. Perugia, D. Schötzau, Recent developments in discontinuous Galerkin methods for the time-harmonic Maxwell's equations, ICS Newsletter 11 (2) (2004) 10–17.
[22] T. Warburton, M. Embree, The role of the penalty in the local discontinuous Galerkin method for Maxwell's eigenvalue problem, Comput. Methods Appl. Mech. Eng. 195 (25–28) (2006) 2305–3223, doi:10.1016/j.cma.2005.06.011.
[23] P. Hansbo, M.G. Larson, Discontinuous Galerkin and the Crouzeix–Raviart element: application to elasticity, Math. Model. Numer. Anal. 37 (1) (2003) 63–72, doi:10.1051/m2an:2003020.
[24] A. Monorchio, A.R. Bretones, R. Mittra, G. Manara, R.G. Martín, A hybrid time-domain technique that combines the finite element, finite difference and method of moment techniques to solve complex electromagnetic problems, IEEE Trans. Antennas Propag. 52 (10) (2004) 2666–2674, doi:10.1109/TAP.2004.834431.
[25] A. Bondeson, G.Y. Fu, Tunable integration scheme for the finite element method, Comput. Phys. Commun. 66 (2–3) (1991) 167–176, doi:10.1016/0010-4655(91)90065-S.
[26] A. Bondeson, T. Rylander, P. Ingelström, Computational Electromagnetics, Springer, New York, NY, 2005.
[27] S. Dey, R. Mittra, Efficient computation of resonant frequencies and quality factors of cavities via a combination of the finite-difference time-domain technique and the Padé approximation, IEEE Microw. Guid. Wave Lett. 8 (12) (1998) 415–417, doi:10.1109/75.746760.
[28] M. Celuch-Marcysiak, W. Gwarek, Generalized TLM algorithms with controlled stability margin and their equivalence with finite-difference formulations for modified grids, IEEE Trans. Microw. Theory Tech. 43 (9) (1995) 2081–2089, doi:10.1109/22.414544.
[29] QWED s.c., Zwyciezcow 34/2, 03-938 Warsaw, Poland, QuickWave-3D FDTD simulator manual, second ed., April 2002.